Temperature dependence of (111) and (110) ceria surface energy

Anastasiia S. Kholtobina,[1,*] Axel Forslund,[2] Andrei V. Ruban,[1,3] Börje Johansson,[1,4] and Natalia V. Skorodumova[1]

[1]*KTH Royal Institute of Technology, Brinellvagen 23, SE-100 44 Stockholm, Sweden*

[2]*Institute for Materials Science, University of Stuttgart, 70569 Stuttgart, Germany*

[3]*Materials Center Leoben Forschung GmbH, Roseggerstraße 12, A-8700 Leoben, Austria*

[4]*Department of Physics and Astronomy, Division of Materials Theory, Uppsala University, 751 20 Uppsala, Sweden*

(Received 19 October 2022; revised 1 December 2022; accepted 5 December 2022; published 12 January 2023)

High-temperature properties of ceria surfaces are important for many applications. Here, we report the temperature dependencies of surface energy for (111) and (110) CeO_2 obtained in the framework of the extended two-stage up-sampled thermodynamic integration using Langevin dynamics. The method was used together with machine-learning potentials called moment tensor potentials (MTPs), which were fitted to the results of the *ab initio* molecular dynamics calculations for (111) and (110) CeO_2 at different temperatures. The parameters of MTP training and fitting were tested, and the optimal algorithm for the ceria systems was proposed. We found that the temperature increases from 0 to 2100 K led to the decrease of the Helmholtz free energy of (111) CeO_2 from 0.78 to 0.64 J/m^2. The energy of (110) CeO_2 dropped from 1.19 J/m^2 at 0 K to 0.92 J/m^2 at 1800 K. We show that it is important to consider anharmonicity, as simple consideration of volume expansion gives the wrong temperature dependencies of the surface energies.

DOI: 10.1103/PhysRevB.107.035407

I. INTRODUCTION

Due to its attractive redox, catalytic, electronic, and mechanical properties, ceria (CeO_2) has become a key material in many modern technologies [1–6]. Automobile exhaust gas catalysts [1,2], solid oxide fuel cells [5,6], and oxygen storage [7] largely rely on the surface properties of ceria [8]. In these applications, ceria works at elevated temperatures [7], and therefore, the knowledge of the thermodynamic properties of ceria surfaces at high temperatures is of great importance. Such information, however, is still limited; even data about the energy of different crystallographic surfaces of ceria are scarce. At the same time, experimental information regarding the properties of bulk ceria is available for different temperatures. For example, ceria heat capacity obtained for the temperature range of 2–900 K using adiabatic scanning calorimetry and differential scanning calorimetry (DSC) has been reported in several studies [9–13]. High-temperature enthalpy data for bulk ceria in the temperature range of 391–1800 K can also be found in the literature [14–16]. Additionally, Hisashige *et al.* [17] have measured the thermal expansion of ceria by thermomechanical analysis in the temperature range from 100 to 800 K and the Debye temperature at room temperature by an ultrasonic pulse method.

During the past decade, several *ab initio* studies devoted to the high-temperature thermodynamic properties of bulk CeO_2 were published [7,13,18–20]. The self-consistent *ab initio* lattice dynamical method [19], which includes the effects of phonon-phonon interactions using the quasiharmonic approximation (QHA), provided a description of phonon and thermodynamic properties of bulk ceria at temperatures from 0 K up to 1500–1800 K [21]. Based on the QHA method and phonon calculations, the thermodynamic properties, such as heat capacity, isothermal bulk modulus, Gibbs free energy, and coefficient of thermal expansion of CeO_2 polymorphs, were obtained in the temperature range of 0–1150 K [20]. Morrison *et al.* [13] calculated the entropy, enthalpy, and Gibbs functions for bulk ceria at temperatures between 5 and 400 K using the Perdew-Burke-Ernzerhof parameterization revised for solids (PBE_{sol}) and the simple Debye model [13]. The obtained Debye temperature (Θ_D), 455 K [13], was in between the previously reported experimental data: 409 K [22], 480 K [17], and reported theoretical values of 481 K [23], 414.5–582.9 K [24]. Additionally, Klarbring *et al.* [7] used the temperature-dependent effective potential method to investigate several high-temperature properties of ceria including thermal expansion [25,26]. Using PBEsol+U, Weck and Kim [23] obtained the crystalline parameters of CeO_2 in good agreement with the experimental values. They also calculated the Debye temperatures within the Voigt-Reuss-Hill approximation. Niu *et al.* [24] obtained the pressure and temperature dependences of the specific heat, Debye temperature, and the thermal expansion coefficient for cubic CeO_2 from the Debye-Grüneisen model.

The information about ceria surfaces at elevated temperatures is scarce in experimental publications and totally nonexistent in theoretical reports. Zouvelou *et al.* [27]

*anastasiia.kholtobina@gmail.com

described an experimental determination of the surface energies of polycrystalline CeO_2 in the argon atmosphere in the 1473–1773 K temperature range, which were measured to be 1.64–1.47 J/m^2. Hayun *et al.* [28] determined the surface energy of nanoceria for hydrated and anhydrous samples at room temperature to be 0.81 and 1.16 J/m^2, respectively. Hayun *et al.* [28] concluded that these surface energies could be attributed to the (111) surface. This assumption was based on the systematic study of the CeO_2 nanoparticles of different sizes using high-resolution transmission electron microscopy [29] and the work by Vyas *et al.* [30] showing that CeO_2 equilibrium morphologies are dominated by the (111) facets.

Here, we report the calculated free energies of the (111) and (110) ceria surfaces at temperatures up to 2100 K. The values were calculated with the extended two-stage upsampled thermodynamic integration using Langevin dynamics (TU-TILD) method [31,32]. This method was previously applied in the free energy calculations of various metallic systems, including vacancy formation free energies [33], stacking fault free energies [31], as well as the surface free energy of TiN [34] and W [35]. In this paper, TU-TILD is combined with machine learning (ML) potentials, particularly the moment tensor potentials (MTPs) [36], which were trained on the results of *ab initio* molecular dynamics (AIMD) calculations [37].

II. METHODS

The methodology of the TU-TILD was applied in this paper to determine the Helmholtz free energies of the ceria bulk and surface supercells and consequently the surface free energies of (111) and (110) ceria.

A. Surface free energy

The slab technique was used to determine the surface free energy γ as

$$\gamma(T) = \frac{F_{\text{slab}}(a_T, T) - F_{\text{bulk}}(a_T, T)}{2A_T}, \tag{1}$$

where $F_{\text{bulk}}(a_T, T)$, and $F_{\text{slab}}(a_T, T)$ refer to the Helmholtz free energies of the slab and bulk calculated for the same number of formula units, respectively; a_T is the lattice constant at temperature T and zero pressure, and A_T is the surface area of the slab. Factor $\frac{1}{2}$ accounts for the two surfaces of the slab.

The Helmholtz free energies of both bulk and surface supercells (subscripts are omitted in the formula) can be adiabatically decomposed into the following contributions:

$$F(a_T, T) = E(a_T) + F^{\text{vib}}(a_T, T), \tag{2}$$

where E denotes the conventional 0 K total energy of the system (either bulk or slab) and F^{vib} the vibrational free energy of the lattice, obtained in the fully anharmonic form using the TU-TILD method.

B. Anharmonic free energy calculations

We applied the TU-TILD method, which treats the interatomic potential as an intermediate reference potential in the thermodynamic integration. The thermodynamic integration is split into two stages: first, from the harmonic to the reference potential and, secondly, from the reference potential to full density functional theory (DFT) [35]. In the framework of this paper, a modified version of the original TU-TILD method was utilized. The first modification was the usage of an optimized Einstein crystal as the analytic reference to compute the absolute free energy, instead of a quasiharmonic reference. The Einstein crystal is a simple and convenient workaround [38]. The corresponding Einstein frequency can be chosen quite arbitrarily within a reasonable interval specific for this system. Since the Einstein system is used only as an auxiliary reference for thermodynamic integration, the choice does not affect the final result obtained after the integration. The second modification of the original TU-TILD method implemented here was the usage of a ML potential, namely, the MTP, as an efficient bridge between the analytical reference system and the DFT system.

Following this formalism [32,39], the full vibrational free energy including the anharmonic is obtained as follows:

$$F^{\text{vib}} = F^{\text{Einst}} + F^{\text{Einst}\to\text{MTP}} + F^{\text{MTP}\to\text{DFT}}, \tag{3}$$

where

$$F^{\text{Einst}\to\text{MTP}} = \int_0^1 d\lambda_1 \langle E^{\text{MTP}} - E^{\text{Einst}} \rangle_{\lambda_1}, \tag{4}$$

$$F^{\text{MTP}\to\text{DFT}} = \int_0^1 d\lambda_2 \langle E^{\text{DFT}} - E^{\text{MTP}} \rangle_{\lambda_2} + \langle \Delta E \rangle^{\text{UP}}, \tag{5}$$

where F^{Einst} is the free energy of an optimized Einstein crystal; E^{Einst}, E^{MTP}, and E^{DFT} are the energies of a particular atomic configuration calculated for the Einstein crystal, calculated with the MTP [40] as implemented in the MLIP software [36], and calculated with low-converged DFT parameters, respectively; and $\langle \ldots \rangle_\lambda$ denote the thermodynamic average for coupling constant λ at certain temperature and volume. Finally, $\langle \Delta E \rangle^{\text{UP}}$ is obtained within the free-energy perturbation theory, and it accounts for the free energy difference between the low- and well-converged DFT calculations [32].

C. ML potentials

MTPs are the class of ML potentials proposed by Shapeev for single-component materials [40] and later extended to multicomponent systems [41]. MTPs are efficient in combination with the TU-TILD method [1,2]. In the framework of ML methods, each considered model should be optimized. To avoid overfitting or underfitting during potential training, the root mean square errors (RMSEs), calculated between the reference outputs and model predictions, were compared at the end of the training process [42].

MTPs represent the energy of an atomic configuration as a sum of the contributions of the local atomic environments of each atom i:

$$E_{\text{tot}}^{\text{MTP}} = \sum_{i=1}^{n} E_i, \tag{6}$$

where each contribution E_i is linearly expanded via a set of basis functions:

$$E_i = \sum_{\alpha} \xi_{\alpha} B_i^{\alpha}, \tag{7}$$

where $\xi = \{\xi_{\alpha}\}$ are parameters to be found by fitting to the training set.

To train MTPs, an active learning technique can be applied in the framework of the MLIP package [36]. This technique allows one to entrust training set refinement iterations to the computer, thus completely automating the training set construction. A good training set should include all representative structures, so that the potential does not have to extrapolate while searching for stable phases. This goal can be achieved by treating the active learning technique as a generalization of the algorithm proposed for linearly parametrized models by Gubaev *et al.* [43] and Novikov and Shapeev [44].

The full iteration of the active learning algorithm consists of five steps [36]:

(1) The training set is constructed from well-converged configurations obtained in DFT-AIMD calculations at the considered temperature.

(2) The pretraining procedure is implemented for an untrained MTP with the defined MTP level and cutoff radius to define the current MTP the first time (MTP renewed at each iteration).

(3) The simulation with the current MTP is performed using the LAMMPS-MLIP interface, and the extrapolative configurations are selected; the simulation is stopped when the maximum extrapolation grade [3] is exceeded, and an update of the training set is performed.

(4) Should new configurations be added to the training set, the total energies of these configurations are calculated with DFT-AIMD and then added to the trained set.

(5) The MTP is retrained using the updated training set.

The whole procedure should be repeated until no new configurations appear in the third step. If only the first two steps are used, we call such a procedure *passive* learning or training since the training set in this case is generated manually and the MTP is not adding any new configurations [36].

III. COMPUTATIONAL DETAILS

The DFT calculations were performed using the projector augmented wave (PAW) method [45] as implemented in the Vienna *Ab initio* Simulation Package (VASP) [46]. The exchange and correlation effects were treated using the PBE_{sol} [47] parametrization of the generalized gradient approximation.

Weck and Kim [23] previously demonstrated that PBE_{sol} described the experimental crystalline parameters and properties of CeO_2 and Ce_2O_3 with good accuracy. For our purpose, the description of cerium oxides within the DFT+U formalism is sufficient [48]. Therefore, the calculations were performed using $PBE_{sol} + U$ energy functional with the Hubbard parameter U of 5 eV applied to the $4f$ states of ceria. The PAW potentials with the following electronic configurations were used: Ce $4s4p4f5d6s$ and O $2s2p$. All calculations were spin polarized with the initial ferromagnetic spin arrangement. The equilibrium lattice parameter of ceria obtained with PBEsol+U was 5.40 Å (0 K), in fair agreement with the experimental value [27].

A. Bulk free energy calculations

The Helmholtz free energy of the bulk system $F_{\text{bulk}}(a_T, T)$ was obtained using Eq. (2). The convergence parameters were chosen to achieve the accuracy of 1 meV/atom or below. The 0 K total energy E_{bulk} (a_T) was calculated for the 96-atom supercell built as a 2×2×2 replication of the 12-atom cubic cell. The total energies were computed for the 12 volumes, with equilibrium at different elevated temperatures [7]. For elevated temperatures, we used the lattice parameters determined in our previous work [7], which were in good agreement with earlier experimental [25,26] and theoretical data [24]. The plane-wave cutoff was set to 500 eV, and the k-point mesh was 2×2×2 [49]. The vibrational free energy $F_{\text{bulk}}^{\text{vib}}(a_T, T)$ was calculated by the TU-TILD method. The procedure of this calculation consisted of the following three steps:

(1) AIMD runs performed in VASP at 12 temperatures from 450 to 2100 K with 150 K steps,

(2) 12 MTPs training in the framework of the active learning algorithm, and

(3) TU-TILD with 12 trained MTPs for each considered temperature.

The thermodynamic integration [step (3)] includes the following substeps corresponding to Eqs. (3)–(5):

(a) calculations of MTP correction to the Einstein crystal model,

(b) calculations of the DFT correction to the MTP free energy, and

(c) additional calculations for the up-sampling term.

All 12 AIMD simulations were run with the Langevin thermostat [50] with the damping parameter of 0.01 fs^{-1}. The van Gunsteren–Berendsen algorithm [51] was used for the integration of Newton's equations of motion. A 1-fs time step was determined to be sufficient for AIMD runs. Each MD run was done for 6000 steps.

For every temperature, we trained the MTP to reproduce the energy and forces of the 6000 atomic configurations for bulk ceria obtained from DFT-AIMD. We did it always in the framework of the active learning approach. The 16th level of the MTP and 5-Å cutoff radius were chosen. The resulting RMSE of the energy difference between DFT and the MTP was 1.6 meV/atom, and the RMSE of the force was 0.51 eV $Å^{-2}$, demonstrating a satisfactory reproducibility of the DFT energies and forces by the fitted MTPs.

Having fitted MTPs for the 12 considered temperatures, we could start the TU-TILD [Eqs. (3)–(5)]. The $F^{\text{Einst}\to\text{MTP}}$ correction was obtained for the 324-atom supercell built as the 3×3×3 replication of the 12-atom cubic cell. The convergence of the free energy correction was <1 meV/atom for all temperatures. It might be important to use a large enough supercell in this integration to capture the contribution of the long-wavelength phonons. At every temperature, a dense set of 26 λ_1 values was used for the integration in Eq. (4). For each λ_1, LAMMPS MD runs up to 50 000 steps were performed to get statistically well-converged results.

The $F^{\mathrm{MTP}\rightarrow\mathrm{DFT}}$ correction was obtained using the 96-atom supercell. Due to a high computational cost of the calculations at this step, only five λ_2 values (0, 0.25, 0.5, 0.75, and 1) were chosen for the integration in Eq. (5). For each λ_2, one MD run with 1000 MD steps was performed. This sampling resulted in a statistical error <0.2 meV/atom, demonstrating the excellent performance of the MTP in reproducing the DFT values. Term E^{DFT} in Eq. (5) was calculated using the plane-wave cutoff of 500 eV and the 2×2×2 Monkhorst-Pack [49] k-point mesh for the 2×2×2 supercell. The calculations of the up-sampling term in Eq. (5), $\langle\Delta E\rangle^{\mathrm{UP}}$, were carried out with the plane-wave cutoff of 700 eV and the 4×4×4 k-point mesh. It appeared that it was enough to perform 10 up-sampling calculations at each temperature to obtain highly converged energies.

B. Slab free energy calculations

The Helmholtz free energy of the surface slab $F_{\mathrm{slab}}(a_T, T)$ was obtained using Eq. (2). All the parameters were converged to the accuracy of 1 meV/atom. The 0 K energy $E_{\mathrm{slab}}(a_T)$ was calculated for the two (111) surface supercells: 2×2 and 4×4 in the xy directions, both with the thickness of 9 layers, containing 36 and 144 atoms, respectively. The (110) CeO_2 supercell was 2×1 in the xy direction with the thickness of 7 layers (42 atoms). The vacuum was 15 Å thick in all cases. The Monkhorst-Pack [49] k-point meshes of 2×2×1 and 4×4×1 were used for 4×4 and 2×2 (111) supercells, respectively. For the (110) 2×1 supercell, 4×6×1 k-point mesh was used. The plane-wave cutoff was 500 eV in all surface calculations.

To calculate $F^{\mathrm{vib}}_{\mathrm{slab}}(a_T, T)$, MTPs for the surface slabs were fitted in the same manner as bulk MTPs. The initial DFT-AIMD runs were performed for 12 temperatures in the range of 450–2100 K for the (111) slab and for 7 temperatures in the range of 600–1800 K for the (110) slab. For slab MTPs, just like for bulk MTPs, the 16th level and cutoff radius of 5 Å were chosen. At each temperature, the slab MTPs were trained to the energies and forces of the 6000 atomic configurations obtained in DFT-AIMD runs. The active learning algorithm of MTP training was applied, just like in the case of bulk MTPs. The resulting RMSE of the energy difference between DFT and the MTP was 0.3–0.5 meV/atom, and the RMSE for the force was 0.04−0.08 eV Å^{-2}.

For the surface correction, $F^{\mathrm{Einst}\rightarrow\mathrm{MTP}}$ was calculated using the (111) 4×4 and (110) 4×8 supercells containing 512 and 672 atoms, respectively. All other parameters were set like for the respective bulk calculations. Correction $F^{\mathrm{MTP}\rightarrow\mathrm{DFT}}$ for surface slabs was obtained using (111) 4×4 and (110) 4×2 supercells containing 144 and 168 atoms, respectively. The same set of λ_2 values (0, 0.25, 0.5, 0.75, and 1) as for the corresponding bulk calculations was used here. At each λ_2, 1000 step MD runs were carried out with the following DFT parameters: the plane-wave cutoff energy of 500 eV and the 2×2×1, 4×4×1 Monkhorst-Pack [49] k-point meshes for the (111) 4×4 and (110) 4×8 supercells. For up-sampling, the following parameters were used: cutoff energy of 700 eV and 6×6×1 and 4×4×1 k-point meshes for 36 and 144 atomic (111) CeO_2 supercells, respectively, and the 6×8×1 k-point mesh for the 42-atom (110) CeO_2 cell. Finally, the surface free energy was calculated according to Eq. (1).

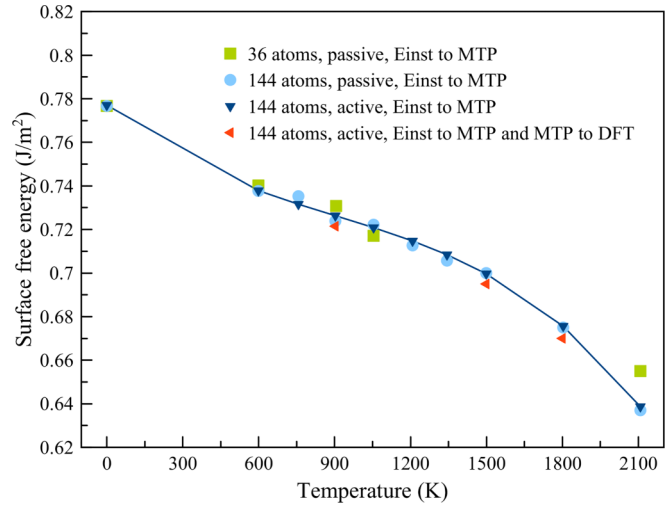

FIG. 1. The surface free energy of (111) ceria surface as the function of temperatures for different supercell sizes, type of moment tensor potential (MTP) training, and corrections to the free energy (Einst → MTP and MTP → DFT). Green squares: $\gamma^{\mathrm{Einst}} + \gamma^{\mathrm{Einst}\rightarrow\mathrm{MTP}}$ for the 36-atom unit cell with MTPs obtained from the passive learning procedure; blue circles: $\gamma^{\mathrm{Einst}} + \gamma^{\mathrm{Einst}\rightarrow\mathrm{MTP}}$ for the 144-atom unit cell with MTPs trained using passive learning; blue triangles: $\gamma^{\mathrm{Einst}} + \gamma^{\mathrm{Einst}\rightarrow\mathrm{MTP}}$ for the 144-atom unit cell with MTPs obtained from active learning; and orange triangles: $\gamma_{\mathrm{tot}} = \gamma^{\mathrm{Einst}} + \gamma^{\mathrm{Einst}\rightarrow\mathrm{MTP}} + \gamma^{\mathrm{MTP}\rightarrow\mathrm{DFT}}$ for the 144-atom unit cell using MTPs obtained from active learning.

IV. RESULTS AND DISCUSSION

Here, we present the results of the application of the above-described methodology to the (111) and (110) ceria surfaces. The temperature dependence of the surface free energy for (111) CeO_2 including full anharmonic vibrational contribution is shown in Fig. 1.The surface energy decreases from 0.78 J/m^2 at 0 K to 0.63 J/m^2 at 2100 K.

In Fig. 1, we compare results obtained for 36- and 144-atom supercells. It is obvious that, already, the 36-atom cell allows one to get reasonably accurate results up to high temperatures. Our tests done for the 144-atom cell show that the surface energy does not change whether we use the "active" or "passive" learning procedure for MTP training (Fig. 1). Based on this finding, only the last variants of MTPs were used for the 36-atom cell to reduce computational cost. Notice that the data in Fig. 1 also show that, in this case, neither the computationally expensive MTP → DFT correction ($\gamma^{\mathrm{MTP}\rightarrow\mathrm{DFT}}$ including the up-sampling procedure) causes any change. This might be explained by a rather high accuracy of our initial MD calculations used to train MTPs in comparison with those used in previous works [34,35], where only the Γ point and a rather low cutoff energy were used. Therefore, it is not surprising that the authors of Ref. [35] obtained a significant MTP → DFT correction, providing a noticeable contribution to the final surface free energy.

Based on our tests performed for the (111) surface, we decided to use a 42-atom cell and passive training for MTPs

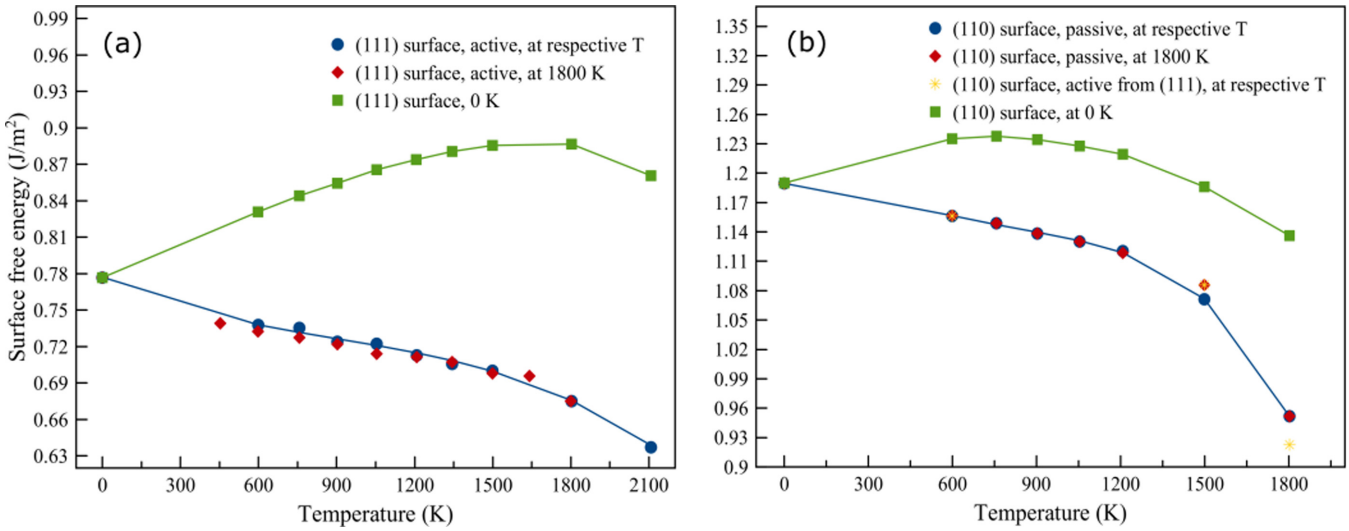

FIG. 2. Surface energies calculated for (a) (111) and (b) (110) ceria surfaces as a function of the temperature. Green squares: Without moment tensor potentials (MTPs) at 0 K using lattice parameters respective to finite temperatures. Blue circles: Using the MTPs of corresponding surfaces at respective finite temperatures. Red diamonds: Using the 1800 K MTPs of corresponding surfaces. Yellow stars: Using the MTPs trained for the (111) surface but applied for the (110) surface at respective finite temperatures.

in our calculations for the (110) surface. The MTP → DFT correction $\gamma^{\mathrm{MTP}\rightarrow\mathrm{DFT}}$ was also neglected. The results for (110) CeO_2 are shown in Fig. 2(a). Figure 2(b) presents the surface energy dependence for (111) CeO_2. The (110) surface free energy decreases from 1.19 J/m^2 at 0 K to 0.92 J/m^2 at 1800 K. Thus, the surface energy decreases between 0 and 1800 K are 0.27 J/m^2 for (110) CeO_2 and 0.15 J/m^2 for the close-packed (111) surface for the same temperature interval. We notice that it is necessary to consider anharmonicity to adequately describe temperature dependence of ceria surface energy. To demonstrate this point, Figs. 2(a) and 2(b) show the surface energies calculated at 0 K for the volumes corresponding to the considered temperatures.

Figures 2(a) and 2(b) also present the results of our transferability tests of the obtained MTPs. The following two types of transferability tests were performed:

(1) The use of the MTP trained at 1800 K for the evaluation of the surface free energy at lower temperatures. This test was applied for both ceria surfaces. MTPs trained at 1800 K [Figs. 2(a) and 2(b)] demonstrate good agreement with the results obtained with the MTPs trained at each corresponding temperature [Figs. 2(a) and 2(b)] both for (111) and (110). The conclusion can be drawn that, at least in the case of ceria surfaces, it is enough to train the MTP at a high temperature and apply it for a range of lower temperatures to estimate the surface free energy with reasonable accuracy.

(2) The use of the individual MTP trained at a particular temperature for (111) ceria for the description of surface free energy of (110) ceria at the same temperature [Fig. 2(b)]. In this case, the best agreement can be found at lower temperatures, for example, 600 K, but this approach still can be used for a rough and quick estimation of the (110) surface free energy even at high temperatures.

Additionally, we tried to use the MTP trained for the (110) surface to describe the (111) surface. This attempt, however, showed no good results even for low temperatures. We note that the MTPs trained for the bulk provided no reasonable description of the (111) or (110) surface.

Finally, we have shown that the calculation of surface free energy without vibrational contribution to Helmholtz free energy gives us quite different values than the one we obtained considering all contributions [green curves in Figs. 2(a) and 2(b)].

The calculated surface energies can be compared with the available experimental data. Hayun *et al.* [28] reported the surface energy value of 0.81 J/m^2 at room temperature, which is in fair agreement with our 0 K value for the (111) surface [Fig. 2(b)]. Zouvelou *et al.* [27] reported the surface energy of polycrystalline CeO_2 to be 1.116–0.998 J/m^2 in the 1473–1773 K temperature range; thus, the surface energy decrease in this temperature interval is ∼0.12 J/m^2 [27]. Note that the type of surface was not specified in Ref. [27].

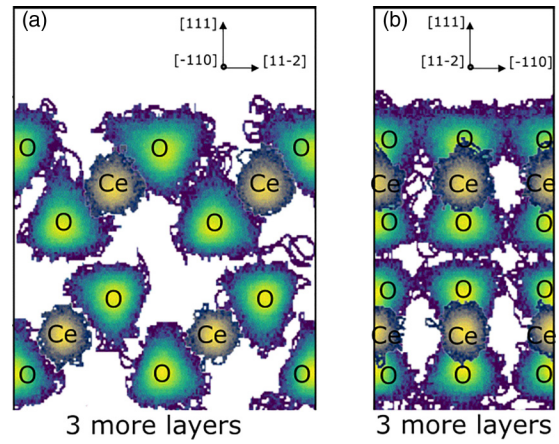

FIG. 3. Atomic trajectories plotted for the (111) surface at 1800 K. (a) Projection from the [−110] direction. (b) Projection from the [11–2] direction. Oxygen atoms are green and cerium atoms are yellow.

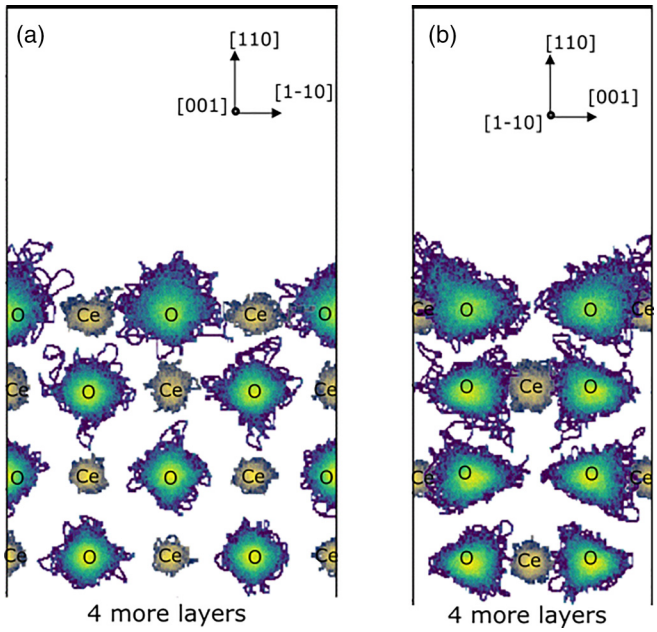

FIG. 4. Atomic trajectories for the (110) ceria surface at 1800 K. (a) Projected along the in-plane [001]. (b) Projected along the in-plane [110]. Oxygen atoms are green, and cerium atoms are yellow.

Figures 2(a) and 2(b) demonstrate that, for both surfaces, the free energy decreases in the temperature interval of 1500–1800 K. However, in the case of the (111) surface, the modest difference of 0.03 J/m^2 was obtained, whereas for the (110) surface, it was 0.12 J/m^2, in good agreement with results by Zouvelou *et al.* [30].

Figures 3 and 4 present the trajectories of oxygen and ceria atoms in (111) and (110) surface slabs, respectively, obtained from 50 000-step MD runs at 1800 K. For both surfaces, as expected, the mobility of surface atoms is larger than that of the bulk atoms. Oxygen atoms shift much further from their crystallographic sites than heavy cerium atoms. In the fluorite structure of ceria, each oxygen is placed in the middle of a tetrahedron of four cerium atoms. The oxygen atom movement is easier through the facet of the cerium tetrahedron than through its edge between two Ce atoms. Under some projection angles, Figs. 3 and 4 demonstrate the characteristic triangular shape of the trajectory distributions.

V. CONCLUSIONS

We demonstrated that the proficient methodology for computing the fully anharmonic surface free energy from *ab initio* calculations based on the TU-TILD method can be successfully applied to oxide surfaces, particularly to CeO_2 (111) and (110) surfaces. The optimal algorithm for the surface free energy calculation in the case of ceria systems has been proposed. It has been shown that, for the considered ceria systems, active training of the MTPs and utilizing of the increased supercell sizes can be excessive if the original MD calculations are performed with reasonably high accuracy. We have also found that MTP-DFT correction and the upsampling term can be neglected for ceria surfaces, again if the initial MD calculations have more k-points than just the Γ point and the cutoff energy of 500 eV. The surface free energy changes from 0.78 J/m^2 at 0 K to 0.64 J/m^2 at 2100 K in the case of CeO_2 (111) and from 1.19 J/m^2 at 0 K to 0.92 J/m^2 at 1800 K in the case of the (110) surfaces. The obtained results are in reasonable agreement with the experimental data by Zouvelou *et al.* [27] and Hayun *et al.* [28]. It is essential to consider anharmonic contributions to adequately describe the temperature dependence of the surface free energy of ceria.

ACKNOWLEDGMENTS

The computations were enabled by resources provided by the Swedish National Infrastructure for Computing (SNIC) at the High Performance Computing Center North and National Computer Center at Linköping University partially funded by the Swedish Research Council (VR-RFI) and through Partnership for Advanced Computing in Europe (PRACE) resources. We acknowledge SNIC and PRACE for awarding us access to Tetralith, Sweden, (Projects No. SNIC 2021/3-36, No. SNIC 2022/1-30, and No. SNIC 2022/22-106), ARCHER 2, United Kingdom (Project No. P2021CEO2SB), and Karolina, Czech Republic (Project No. EU2010PA6106), respectively. B.J., N.V.S., and A.S.K. acknowledge the financial support from the Carl Trygger Foundation (CTS 20-206). A.F. acknowledges funding from the European Research Council (ERC) under the EUs Horizon 2020 Research and Innovation Program (Grant Agreement No. 865855). A.V.R. also gratefully acknowledges the financial support under the scope of the COMET program within the K2 Center Integrated Computational Material, Process and Product Engineering (IC-MPPE; Project No. 859480). This program is supported by the Austrian Federal Ministries for Climate Action, Environment, Energy, Mobility, Innovation and Technology and for Digital and Economic Affairs, represented by the Austrian research funding association and the federal states of Styria, Upper Austria, and Tyrol. We are also thankful to Blazej Grabowski for providing software for thermodynamic integration.

[1] M. S. Dresselhaus and I. L. Thomas, Alternative energy technologies, Nature (London) **414**, 332 (2001).

[2] S. Song, X. Wang, and H. Zhang, CeO_2-encapsulated noble metal nanocatalysts: Enhanced activity and stability for catalytic application, NPG Asia Mater **7**, e179 (2015).

[3] H. J. Beie and A. Gnörich, Oxygen gas sensors based on CeO_2 thick and thin films, Sens. Actuators B Chem. **4**, 393 (1991).

[4] A. Goyal, M. P. Paranthaman, and U. Schoop, The RABiTS approach: using rolling-assisted biaxially textured substrates for high-performance YBCO superconductors, MRS Bull. **29**, 552 (2004).

[5] D. J. L. Brett, A. Atkinson, N. P. Brandon, and S. J. Skinner, Intermediate temperature solid oxide fuel cells, Chem. Soc. Rev. **37**, 1568 (2008).

[6] S. Park, J. M. Vohs, and R. J. Gorte, Direct oxidation of hydrocarbons in a solid-oxide fuel cell, Nature (London) **404**, 265 (2000).

[7] J. Klarbring, N. V. Skorodumova, and S. I. Simak, Finite-temperature lattice dynamics and superionic transition in ceria from first principles, Phys. Rev. B **97**, 104309 (2018).

[8] N. V. Skorodumova, M. Baudin, and K. Hermansson, Surface properties of CeO_2 from first principles, Phys. Rev. B **69**, 075401 (2004).

[9] E. F. Westrum Jr. and A. F. Beale Jr., Heat capacities and chemical thermodynamics of cerium(III) flouride and of cerium(IV) oxide from 5 to 300° K, J. Phys. Chem. **65**, 353 (1961).

[10] I. Riess, M. Ricken, and J. Nölting, On the specific heat of nonstoichiometric ceria, J. Solid State Chem. **57**, 314 (1985).

[11] S. A. Gallagher and W. R. Dworzak, Thermodynamic properties of cerium oxalate and cerium oxide, J. Am. Ceram. Soc. **68**, C-206 (1985).

[12] R. Venkata Krishnan and K. Nagarajan, Heat capacity measurements on uranium-cerium mixed oxides by differential scanning calorimetry, Thermochim. Acta **440**, 141 (2006).

[13] T. D. Morrison, E. S. Wood, P. F. Weck, E. Kim, S. O. Woo, A. T. Nelson, and D. G. Naugle, A comprehensive assessment of the low-temperature thermal properties and thermodynamic functions of CeO_2, J. Chem. Phys. **151**, 044202 (2019).

[14] A. N. Kuznetsov, F. A. Rezukhina, and T. N. Golubenko, Determination of the heat of formation of cerium (III) oxide by combustion in a bomb calorimeter, Russian J. Phys. Chem. **34**, 1010 (1960).

[15] E. G. King and A. U. Christensen, *High-Temperature Heat Contents and Entropies of Cerium Dioxide and Columbium Dioxide* (US Dept. of the Interior, Bureau of Mines, Washington, DC, 1961).

[16] T. S. Yashvili, D. Sh. Tsagareishvili, and G. G. Gvelesiani, Enthalpy and heat capacity of the yttrium sesquioxide and cerium dioxide at high temperatures, Soobshch. Akad. Nauk Gruz. SSR **46**, 409 (1967).

[17] T. Hisashige, Y. Yamamura, and T. Tsuji, Thermal expansion and Debye temperature of rare earth-doped ceria, J. Alloys Compd. **408–412**, 1153 (2006).

[18] C. B. Gopal and A. van de Walle, *Ab initio* thermodynamics of intrinsic oxygen vacancies in ceria, Phys. Rev. B **86**, 134117 (2012).

[19] Z. W. Niu, Z. Y. Zeng, C. E. Hu, L. C. Cai, and X. R. Chen, Study of the thermodynamic properties of CeO_2 from *ab initio* calculations: The effect of phonon-phonon interaction, J. Chem. Phys. **142**, 014503 (2015).

[20] Y. X. Yang, S. L. Zhu, Z. F. Zhang, X. H. Liu, L. S. Li, Y. Yu, and X. F. Tian, First-principles calculations of phase transition, elasticity, phonon spectra, and thermodynamic properties for CeO_2 polymorphs, J. Solid State Chem. **307**, 122761 (2022).

[21] K. Clausen, W. Hayes, J. E. Macdonald, R. Osborn, P. G. Schnabel, M. T. Hutchings, and A. Magerl, Inelastic neutron scattering investigation of the lattice dynamics of Tho_2 and CeO_2, J. Chem. Soc. Faraday Trans. 2 **83**, 1109 (1987).

[22] M. Khafizov, I. W. Park, A. Chernatynskiy, L. He, J. Lin, J. J. Moore, D. Swank, T. Lillo, S. R. Phillpot, A. El-Azab *et al.*, Thermal conductivity in nanocrystalline ceria thin films, J. Am. Ceram. Soc. **97**, 562 (2014).

[23] P. F. Weck and E. Kim, Assessing Hubbard-corrected AM05+U and PBEsol+U density functionals for strongly correlated oxides CeO_2 and Ce_2O_3, Phys. Chem. Chem. Phys. **18**, 26816 (2016).

[24] Z. W. Niu, Y. Cheng, H. Y. Zhang, and G. F. Ji, First-principles investigations on structural, phonon, and thermodynamic properties of cubic CeO_2, Int. J. Thermophys. **35**, 1601 (2014).

[25] S. Omar, E. D. Wachsman, J. L. Jones, and J. C. Nino, Crystal structure-ionic conductivity relationships in doped ceria systems, J. Am. Ceram. Soc. **92**, 2674 (2009).

[26] M. Yashima, D. Ishimura, Y. Yamaguchi, K. Ohoyama, and K. Kawachi, High-temperature neutron powder diffraction study of cerium dioxide CeO_2 up to 1770 K, Chem. Phys. Lett. **372**, 784 (2003).

[27] N. Zouvelou, X. Mantzouris, and P. Nikolopoulos, Surface and grain-boundary energies as well as surface mass transport in polycrystalline CeO_2, Mater. Sci. Eng. A **495**, 54 (2008).

[28] S. Hayun, T. Y. Shvareva, and A. Navrotsky, Nanoceria-energetics of surfaces, interfaces and water adsorption, J. Am. Ceram. Soc. **94**, 3992 (2011).

[29] Z. L. Wang and X. Feng, Polyhedral shapes of CeO_2 nanoparticles, J. Phys. Chem. B **107**, 13563 (2003).

[30] S. Vyas, R. W. Grimes, D. H. Gaya, and A. L. Rohlc, Structure, stability and morphology of stoichiometric ceria crystallites, J. Chem. Soc. Faraday Trans. **94**, 427 (1998).

[31] X. Zhang, B. Grabowski, F. Körmann, A. V. Ruban, Y. Gong, R. C. Reed, T. Hickel, and J. Neugebauer, Temperature dependence of the stacking-fault Gibbs energy for Al, Cu, and Ni, Phys. Rev. B **98**, 224106 (2018).

[32] A. I. Duff, T. Davey, D. Korbmacher, A. Glensk, B. Grabowski, J. Neugebauer, and M. W. Finnis, Improved method of calculating *ab initio* high-temperature thermodynamic properties with application to ZrC, Phys. Rev. B **91**, 214311 (2015).

[33] X. Zhang, B. Grabowski, T. Hickel, and J. Neugebauer, Calculating free energies of point defects from *ab initio*, Comput. Mater. Sci. **148**, 249 (2018).

[34] A. Forslund, X. Zhang, B. Grabowski, A. V. Shapeev, and A. v. Ruban, *Ab initio* simulations of the surface free energy of TiN (001), Phys. Rev. B **103**, 195428 (2021).

[35] A. Forslund and A. V. Ruban, *Ab initio* surface free energies of tungsten with full account of thermal excitations, Phys. Rev. B **105**, 045403 (2022).

[36] I. S. Novikov, K. Gubaev, E. V. Podryabinkin, and A. V. Shapeev, The MLIP package: Moment tensor potentials with MPI and active learning, Mach. Learn. Sci. Technol. **2**, 025002 (2021).

[37] B. Grabowski, Y. Ikeda, P. Srinivasan, F. Körmann, C. Freysoldt, A. I. Duff, A. Shapeev, and J. Neugebauer, *Ab initio* vibrational free energies including anharmonicity for multicomponent alloys, npj Comput. Mater. **5**, 80 (2019).

[38] D. Korbmacher, *Ab Initio Study of Strongly Anharmonic and Dynamically Unstable Systems*, Doctoral Dissertation, Ruhr-Universität Bochum, 2019.

[39] A. I. Duff, M. W. Finnis, P. Maugis, B. J. Thijsse, and M. H. F. Sluiter, MEAMFIT: A reference-free modified embedded atom method (RF-MEAM) energy and force-fitting code, Comput. Phys. Commun. **196**, 439 (2015).

[40] A. V. Shapeev, Moment tensor potentials: a class of systematically improvable interatomic potentials, Multiscale Model. Simul. **14**, 1153 (2016).

[41] A. Shapeev, Accurate representation of formation energies of crystalline alloys with many components, Comput. Mater. Sci. **139**, 26 (2017).

[42] S. K. Wallace, A. S. Bochkarev, A. van Roekeghem, J. Carrasco, A. Shapeev, and N. Mingo, Free energy of $(Co_xMn_{1-x})_3O_4$ mixed phases from machine-learning-enhanced *ab initio* calculations, Phys. Rev. Mater. **5**, 035402 (2021).

[43] K. Gubaev, E. V. Podryabinkin, G. L. W. Hart, and A. V. Shapeev, Accelerating high-throughput searches for new alloys with active learning of interatomic potentials, Comput. Mater. Sci. **156**, 148 (2019).

[44] I. S. Novikov and A. V. Shapeev, Improving accuracy of interatomic potentials: more physics or more data? A case study of silica, Mater. Today Commun. **18**, 74 (2019).

[45] P. E. Blöchl, Projector augmented-wave method, Phys. Rev. B **50**, 17953 (1994).

[46] J. Kresse and G. Furthmüller, Efficiency of *ab-initio* total energy calculations for metals and semiconductors using a plane-wave basis set, Comput. Mater. Sci. **6**, 15 (1996).

[47] J. P. Perdew, A. Ruzsinszky, G. I. Csonka, O. A. Vydrov, G. E. Scuseria, L. A. Constantin, X. Zhou, and K. Burke, Restoring the Density-Gradient Expansion for Exchange in Solids and Surfaces, Phys. Rev. Lett. **100**, 136406 (2008).

[48] S. Dudarev and G. Botton, Electron-energy-loss spectra and the structural stability of nickel oxide: an LSDA+U study, Phys. Rev. B **57**, 1505 (1998).

[49] J. D. Monkhorst and H. J. Pack, Special points for Brillouin-zone integrations, Phys. Rev. B **13**, 5188 (1976).

[50] B. Grabowski, L. Ismer, T. Hickel, and J. Neugebauer, *Ab initio* up to the melting point: Anharmonicity and vacancies in aluminum, Phys. Rev. B **79**, 134106 (2009).

[51] W. F. van Gunsteren and H. J. C. Berendsen, Algorithms for brownian dynamics, Mol. Phys. **45**, 637 (1982).